2023 IEEE/ASME International Conference on Advanced Intelligent Mechatronics (AIM)
June 28-30, 2023. Seattle, Washington, USA

Multi-Objective Co-Design for Mission-Specific Development of Unmanned Aerial Systems

Jolan Wauters, Tom Lefebvre and Guillaume Crevecoeur

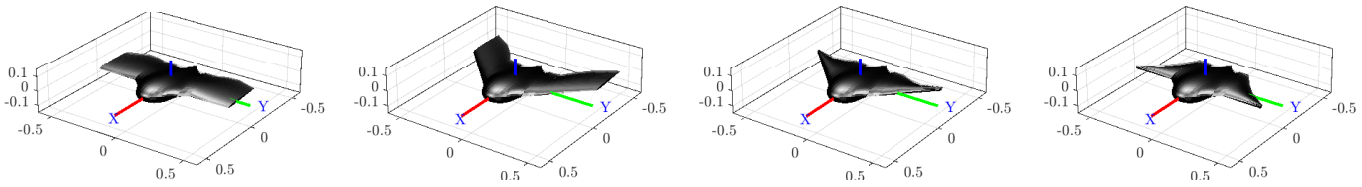

***Abstract*—In recent years, unmanned aerial systems (UAS) are being utilized for a variety of increasingly complex tasks, including the inspection of offshore installations and the transportation of medical equipment. This has motivated the development of mission-specific dynamic design procedures. The principle of concurrent control and design, also known as co-design, extends the traditional approach of design optimization and trajectory optimization by integrating both into a single treatment. This results in coupled solutions that cannot be achieved using a traditional sequential approach. Studies have demonstrated the effectiveness of combining surrogate-assisted optimization methods, such as Bayesian optimization, with a nested formulation of the co-design problem. In the present work, we extend this approach by simultaneously treating multiple objectives. A reformulation of the Bayesian optimization framework through the use of an alternative acquisition function is fit around a trajectory optimization routine. This results in a novel framework that generates optimized designs that outperform the standard design in various metrics. This allows the designer to select a compromising design based on the system's application type and confirms the effectiveness of the concurrent design and control procedure. The subsequent methodology is evaluated on the mission-specific design of a fixed-wing unmanned aerial system, with the aim of conducting a survey mission in challenging terrain. To model the dynamics of the aircraft, the differential flatness of the system is utilized.**

***Index Terms*—Bayesian Optimization, Multi-Objective Optimization, Trajectory Optimization, Co-design, Unmanned Aerial Vehicles, Differential Flatness.**

I. Introduction

Engineering innovation of mechatronic systems demands a corresponding evolution in their model-based system design, which emphasizes the central role of behavioral models in addressing both shape, size and control design concerns. This approach strives for an efficient, cost-effective design process that reduces the need for multiple iterations, ultimately resulting in pioneering systems with enhanced or even novel capabilities. By focusing on model-based system design, the enhancement of functional performance, energy efficiency, and facilitation of autonomous execution of complex tasks, can be pursued.

In the model-based system design paradigm, performance measures as a function of a set of design variables are derived from a model describing the system and optimized. Historically, design optimization, which pertains to the motion-independent attributes of the mechatronic system, and trajectory optimization, which pertains to the motion-motivated control signals made by the system, have been handled as distinct processes. Refer to Fig. 1 for an extended design system matrix representation of the sequential system design approach [1]. The principle of concurrent control and design, or co-design, integrates these approaches by linking design and trajectory optimization. The result of which is an extended design space that permits the development of concurrent static and dynamic optimal designs that are not achievable through a successive design approach, such as maximizing static performance first and enhancing the dynamic abilities without altering the design second [2].

In general, two main architectures can be considered for the integration of design optimization and trajectory optimization in mechatronic systems: (1) a nested approach, in which the optimal trajectory is determined for each iteration of the design optimization problem, and (2) a simultaneous approach, in which the optimal design and trajectory are determined in parallel. The nested approach allows for separate definition of static and dynamic objectives, as well as the use of solvers that are tailored to the specific characteristics of the problem, such as the presence of constraints. However, this approach is also subject to drawbacks, such as feasibility and computational costs. On the other hand, the simultaneous approach is characterized by a reduced number of iterations and computational time, but has a larger and more complex design space [2]. A comparative study of the two architectures was presented in [3].

In this work, we propose a multi-objective co-design framework for the mission-specific design. This is realized by combining a nested co-design problem formulation with a multi-objective Bayesian optimization framework. To validate the newly devised methodology the mission-specific design of a *fixed-wing unmanned aerial system* (FW-UAS) for multiple

J. Wauters, T. Lefebvre and G. Crevecoeur are with the Dynamic Design Lab (D2Lab) of the Department of Electromechanical, Systems and Metal Engineering, Ghent University, B-9052 Ghent, Belgium e-mail: {jolan.wauters, tom.lefebvre, guillaume.crevecoeur}@ugent.be.

J. Wauters, T. Lefebvre and G. Crevecoeur are member of core lab MIRO, Flanders Make, Belgium.

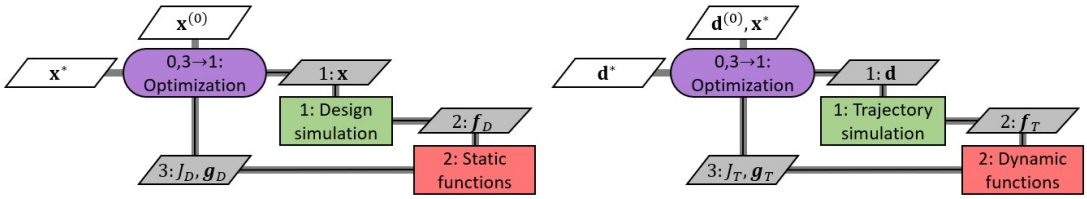

Fig. 1: XDSM (extended design system matrix [1]) representation of the sequential system design approach. The grey lines in the figure depict the flow of data, while the black lines indicate the flow of processes. Horizontal lines denote output and vertical lines denote input. The variables $\mathbf{d}$, $\mathbf{x}$, $\mathbf{f}$, g *and* J *represent the optimization variables, state variables, simulator output, constraints and objective, respectively. The subscripts 'D' and 'T' indicate the distinction between static (design) and dynamic (trajectory) elements, respectively. Superscripts within brackets indicate the iteration number, and a star denotes an optimum value.*

criteria is presented. Generating trajectories for FW-UASs poses a challenge due to its nonlinear underactuated dynamics. An inverse model of the dynamics can be beneficial for trajectory optimization [4]. However, in the absence of such an inverse model and to overcome the issue of underactuation, we employ the differential flatness characteristic of the UAS, as outlined in [5].

The structure of this paper is as follows: In Section II, we present the methodological foundations of the proposed multi-objective mission-specific design procedure, including the discussion of the nested co-design problem and the elaboration on the multi-objective Bayesian optimization approach, which serves as the outer loop of the nested optimization framework. In Section III, we detail the modeling of a FW-UAS using differential flatness, including a description of the aerodynamic solver used to obtain the aerodynamic force coefficients. In Section IV, we demonstrate the application of the proposed approach to the multi-objective mission-specific design of a fixed-wing UAS for challenging surveying tasks. Finally, in Section V, we provide a conclusion and an outlook for future research.

II. Multi-objective Mission Specific Design

In this section we describe the cornerstones of the multi-objective mission specific design procedure by elaborating on the nested co-design problem formulation and the multi-objective Bayesion optimization methodology.

A. Multi-objective nested co-design

The current co-design solution methods build upon existing numerical schemes developed for trajectory optimization, such as those presented in references [6, 7, 8]. These methods typically involve discretizing the trajectory optimization problem using techniques such as *Direct Multiple Shooting* (DMS). This reformulation transforms the problem into a conventional (constrained) numerical optimization problem, which can be tackled using suitable optimizers. With regard to co-design, the optimization variables derived from the trajectory parametrization are extended to include static design variables, resulting in a simultaneous co-design approach. Nevertheless, if the design variables are included as optimization variables, it may result in a less sparse optimization problem. To tackle this problem, a nested co-design architecture can be used. It should be emphasized that in a nested approach, the evaluation of the objective function necessitates solving the entire trajectory optimization problem.

In engineering design problems, conflicting objectives are common. As such, the goal becomes the identification of the set of non-dominated objectives, where improving one objective would lead to the deterioration of another. This (hyper-)surface is known as the Pareto front or Pareto boundary $\mathcal{P} \triangleq \mathrm{Par}(\{\mathbf{J}_1(\mathrm{D}), ..., \mathbf{J}_m(\mathrm{D}) | \mathrm{D} = \mathbf{d}_1, ..., \mathbf{d}_n\})$. In the present study, we use the vector $\mathbf{d}$ to denote the design variables, the state and control signals are represented by $\mathbf{x}$ and $\mathbf{u}$, respectively. The functionals J_D, and J_T represent the static design objective problem, and the dynamic trajectory optimization objective, respectively. The latter is typically expressed as a time integral, as will be discussed in a subsequent section. Furthermore, the dynamics of the system are represented by $\mathbf{f}$, the constraint functions of the trajectory optimization problem are represented by $\mathbf{g}_T$, and the constraint functions of the design optimization problem are represented by $\mathbf{g}_D$. The multi-objective nested co-design problems can be formulated as follows

$$
\begin{aligned}
\mathrm{D}^* = \arg \underset{\mathbf{d} \in \mathrm{D} \subset \mathcal{D}}{\mathrm{Par}} \ & \mathbf{J}_D(\mathbf{d} | \mathbf{x}^*, \mathbf{u}^*) \\
\text{s.t. } & \mathbf{g}_D(\mathbf{d} | \mathbf{x}^*, \mathbf{u}^*) \leq 0 \\
\{\mathbf{x}^*, \mathbf{u}^*\} = \arg \min_{\mathbf{x}, \mathbf{u}} \ & J_T[\mathbf{x}, \mathbf{u} | \mathbf{d}] \\
\text{s.t. } & \dot{\mathbf{x}} = \mathbf{f}(\mathbf{x}, \mathbf{u} | \mathbf{d}), \\
& \mathbf{g}_T(\mathbf{x}, \mathbf{u}; \mathbf{d}) \leq 0
\end{aligned}
\tag{1}
$$

where D represents a set of design vectors and $\mathcal{D}$ represents the design space of interest, often a compact subset of $\mathbb{R}^{d_\mathcal{D}}$. Furthermore, it is assumed that $\mathbf{J}_D : \mathcal{D} \mapsto \mathbb{R}$ are continuous functions that are noise-free and gradient-free, in the sense that a direct evaluation of the gradient is unattainable without approximations. Since the nested co-design formulation demands a trajectory optimization during every design optimization step, the computational burden can become significant. To account for this problem *Bayesian optimization* (BO) can be employed. The central idea of BO to solve this problem is to build a surrogate model of the objective(s) that can be updated and queried to drive the optimization decisions [9].

B. Multi-objective Bayesian Optimization

To determine the Pareto front in the context of *Bayesian optimization* (BO), the state of the art approach is to construct a surrogate model of each of the objective functions and formulate an acquisition function that attempts to improve upon the current best evaluated Pareto front. The most commonly

used surrogate model in the context of BO is the *Gaussian process interpolator*. In accordance to the function-space view a Gaussian process can be defined as a distribution over functions such that the set of values of $J(\mathbf{d})$ evaluated at an arbitrary set of points $\{\mathbf{d}_i | i = 1, ..., N\}$ jointly have a Gaussian distribution. A Gaussian process is fully described by second-order statistics $\mathcal{J}(\mathbf{d}) = \mathcal{GP}(m(\mathbf{d}), \psi(\mathbf{d}, \mathbf{d}'))$, with $m(\mathbf{d}) : \mathcal{D} \mapsto \mathbb{R}$ the mean function and $\psi(\mathbf{d}, \mathbf{d}') : \mathcal{D} \times \mathcal{D} \mapsto \mathbb{R}$ the covariance function. Depending on the formulation of the mean function, different interpolators can be obtained. In case of a constant value the method is referred to as *simple Kriging*, in the case of a multivariate polynomial $\mathbf{f}(\mathbf{d})$, which is used in this work, we refer to the interpolator as *universal Kriging*.

The surrogate model is trained by maximizing the marginal likelihood $\mathcal{L} \triangleq p(\boldsymbol{\theta}|\mathbb{D})$, where $\mathbb{D}$ represents the set of all samples that the surrogate is capable of reproducing. This involves determining the hyperparameters of the covariance function.

Building forth on the definition of a Gaussian process and the theorem of Bayes the predictive distribution $p[\mathcal{J}(\mathbf{d})|J(\mathbb{D})]$ can be directly evaluated and gives again a normal distribution of which the mean $\mathbb{E}[\mathcal{J}(\mathbf{d})] \triangleq \mu(\mathbf{d})$ and variance $\mathbb{V}[\mathcal{J}(\mathbf{d})] \triangleq \Sigma(\mathbf{d})$ can be directly evaluated with $\boldsymbol{\alpha} = \Psi^{-1}(\mathbf{d} - \mathrm{F}\boldsymbol{\beta})$, $\Gamma = (\mathrm{F}^\top \Psi^{-1} \mathrm{F})^{-1}$, $\mathbf{g}(\mathbf{d}) = \mathrm{F}^\top \Psi^{-1} \boldsymbol{\psi}(\mathbf{d}) - \mathbf{f}(\mathbf{d})$.

$$\mu(\mathbf{d}) = \boldsymbol{\beta}^\top \cdot \mathbf{f}(\mathbf{d}) + \boldsymbol{\alpha}^\top \cdot \boldsymbol{\psi}(\mathbf{d}) \tag{2a}$$

$$\Sigma(\mathbf{d}) = \sigma^2 \big\{ \psi(0) - ||\boldsymbol{\psi}(\mathbf{d})||^2_{\Psi^{-1}} + ||\mathbf{g}(\mathbf{d})||^2_{\Gamma} \big\} \tag{2b}$$

with F the model matrix defined by $\mathrm{F}^{(i,j)} = f_i(\mathbf{d}_j)$ and Ψ the correlation matrix defined by $\Psi^{(i,j)} = \psi(\mathbf{d}_i, \mathbf{d}_j)$. The coefficients of the multivariate polynomial trend $\boldsymbol{\beta}$ and the process variance σ^2 are obtained by enforcing stationarity on the log marginal likelihood function.

A commonly employed type of covariance functions in the field aerospace engineering is the Matérn covariance function [10, 11]. It is often preferred over the conventional exponential covariance function, which infinitely differentiable nature leads to nonphysical levels of smoothness [12].

An open-source toolbox called ooDACE (*object-orientated Design and Analysis of Computer Experiments*) [13] is used for constructing the Gaussian process interpolator. A multi-start *sequential quadratic programming* (SQP) approach is employed to optimize the concentrated log marginal likelihood function [14, 15].

The current standard to assess the Pareto set quality is the hypervolume indicator $\mathcal{H}(\mathcal{P})$. The hypervolume (HV) or $\mathcal{S}$-metric corresponds to the Lebesque measure of the hyperspace dominated by the Pareto front bounded by a reference point in the objective space $\mathbf{r} \triangleq \{J_j(\mathbf{x}) | j = 1...m\}$. The indicator can also be used to define a scalar improvement function $\mathcal{I}_{hv}(\mathbf{p}|\mathcal{P}, \mathbf{r})$ which measures the contribution (or improvement) of the point $\mathbf{p} \triangleq \{\mathcal{Y}_j(\mathbf{x}) | j = 1...m\}$ to the Pareto set $\mathcal{P}$. Identical to the single-objective case can the stochastic nature of the interpolator be used to assess the uncertainty in the prediction and evaluated to define the expected hypervolume improvement $\mathbb{E}_{\mathcal{J}}[\mathcal{I}_{hv}(\mathbf{p}|\mathcal{P}, \mathbf{r})]$. We ease out the notation by introducing $\phi_j(\mathbf{x}) \triangleq \phi(\mathcal{J}_j | \mu_j(\mathbf{x}), \Sigma_j(\mathbf{x}))$ with ϕ the standard normal probability density function

$$\mathcal{I}_{hv}(\mathbf{p}|\mathcal{P}, \mathbf{r}) = \max[\mathcal{H}(\mathcal{P} \cup \mathbf{p}|\mathbf{r}) - \mathcal{H}(\mathcal{P}|\mathbf{r}), 0] \tag{3a}$$

$$\mathbb{E}_{\mathcal{J}}[\mathcal{I}_{hv}(\mathbf{p}|\mathcal{P}, \mathbf{r})] = \int \mathcal{I}_{hv}(\mathbf{p}|\mathcal{P}, \mathbf{r}) \prod_{j=1}^{m} \phi_j(\mathbf{x}) d\mathcal{Y}_j \tag{3b}$$

Details on the effective calculation of this criteria can be found in [16].

C. Differentially flat trajectory optimization

Differential flatness refers to a mathematical characteristic found in specific dynamic systems which asserts that the states, represented by the vector $\mathbf{x}$, and control inputs, represented by the vector $\mathbf{u}$, of the system can be described by function of a flat output, represented by the vector $\mathbf{s}$, and its derivatives. The flatness property implies that for a given flat output trajectory represented by $\mathbf{s}(t)$, any feasible state and control input trajectory represented by $\mathbf{x}(t), \mathbf{u}(t)$ that satisfies the dynamic equation of the flat system can be uniquely determined. Therefore, the flat output, represented by the vector $\mathbf{s}$, serves as a minimal representation of the dynamics of the system.

Since the dynamic system under consideration is differentially flat, it is possible to establish a correspondence between any admissible trajectory and its corresponding counterpart in the flat coordinate space. We employ the B-spline framework, as described in [17], to parameterize the flat trajectory $\mathbf{s}(t)$. A function basis known as a B-spline of order d is composed of basis functions represented by piecewise polynomials, denoted as $B_{i,d}$. A knot-vector, a non-decreasing set of time instants $\mathcal{T} = t_0, t_1, \ldots, t_m$, further describes the basis functions. By setting t_0 to 0 and t_m to T, the B-spline covers the time interval $[0, T]$. The total number of basis functions can be determined as $n = m - d + 1$. The flat trajectory can be expressed as a linear combination of the B-spline basis functions and a set of coefficients, $\mathbf{c}_i$, such that $\mathbf{s}(t) = \sum_{i=0}^{n} B_{i,d}(t)\mathbf{c}_i$.

The aim is to minimize an integrand $l(\mathbf{x}, \mathbf{u})$ over a time interval $[0, T]$. Since the integral is nonlinear and not explicitly computable, some researchers prefer to use a linear or quadratic integrand in the flat coordinates to ensure that the integrand is polynomial and explicitly integratible [18]. Rather than using an integral over the entire interval, we use a trapezoidal integration rule on a dense sample grid $\mathcal{G}$. Additionally, inequality constraints can be incorporated to reinforce specific characteristics of the trajectories.

$$\begin{aligned} \mathbf{c}^* = \arg\min_{\mathbf{c}} \sum\nolimits_{t \in \mathcal{G}} l(\Phi[\mathbf{s}](t), \Psi[\mathbf{s}](t)), \ t \in \mathcal{G} \\ \text{s.t. } \mathbf{g}(\Phi[\mathbf{s}](t), \Psi[\mathbf{s}](t)) \leq 0, \ t \in \mathcal{C} \end{aligned} \tag{4}$$

The trajectory optimization problem, formulated as a *nonlinear program* (NLP), is typically solved using standard numerical optimization techniques. In this work, we employ the *sequential quadratic programming* (SQP) method, which is implemented in the `fmincon` environment in Matlab, and utilize default numerical differentiation settings to compute the gradient. It should be noted that due to the presence of inequality constraints and the requirement for numerical gradient evaluations, the solution of the trajectory optimization problem can be computationally intensive. This further highlights the

need for the utilization of efficient optimization methods in the outer loop of a nested co-design framework.

III. Fixed wing UAS modeling

To validate the newly proposed framework, we present the mission-specific design of a FW-UAS for multiple criteria. In this section we describe the different aspects required to evaluate the impact of design and control on mission performance.

A. Rigid body dynamics of flight

The coordinate systems employed in our analysis include the world frame of reference (f.o.r.) $\mathcal{W}$ and the body f.o.r. $\mathcal{B}$, which is fixed to the center of mass of the vehicle. For a visual representation of these different frames of reference, please refer to the accompanying scheme (Fig. 2).

The kinematics of the vehicle can be represented by its relative pose, which is characterized by the homogeneous transformation matrix between the world frame of reference $\mathcal{W}$ and the body frame of reference $\mathcal{B}$, denoted by ${}^{\mathcal{W}}_{\mathcal{B}}\mathrm{T} \in \mathfrak{SE}(3)$. This matrix is determined by a translation vector ${}^{\mathcal{W}}_{\mathcal{B}}\mathbf{p} \in \mathbb{R}^3$, which characterizes the position of $\mathcal{B}$ relative to $\mathcal{W}$, and a rotation matrix ${}^{\mathcal{W}}_{\mathcal{B}}\mathrm{R} \in \mathfrak{SO}(3)$, which characterizes the orientation of $\mathcal{B}$ relative to $\mathcal{W}$. The differential kinematics of the vehicle are given by ${}^{\mathcal{W}}_{\mathcal{B}}\dot{\mathbf{p}} = {}^{\mathcal{W}}_{\mathcal{B}}\mathbf{v}$ and ${}^{\mathcal{W}}_{\mathcal{B}}\dot{\mathrm{R}} = {}^{\mathcal{W}}_{\mathcal{B}}\mathrm{R}\,{}^{\mathcal{W}}_{\mathcal{B}}\Omega$, where $\Omega = \hat{\boldsymbol{\omega}}$.

To simplify the modeling, a minimal representation $\mathbf{q} \in \mathbb{R}^3$ is used for the rotation matrix ${}^{\mathcal{W}}_{\mathcal{B}}\mathrm{R}$. This allows the definition of the rotation matrix as ${}^{\mathcal{W}}_{\mathcal{B}}\mathrm{R}(\mathbf{q})$, and the local angular velocities as ${}_{\mathcal{B}}\boldsymbol{\omega} = {}_{\mathcal{B}}\mathrm{J}(\mathbf{q})\dot{\mathbf{q}}$, where $\dot{\mathbf{q}} = {}_{\mathcal{B}}\mathrm{J}(\mathbf{q})^{-1}\boldsymbol{\omega}$. This numerical modeling approach is valid as long as the flight trajectories are not close to the singularities of the Jacobian matrix, ${}_{\mathcal{B}}\mathrm{J}(\mathbf{q})$. We adopt the yaw-roll-pitch (ψ, ϕ, θ) convention in a ZXY rotation sequence and we make the assumption that the vehicle meets the requirements that define a rigid body, and hence, the dynamics of the vehicle are governed by the Newton-Euler equations.

The aerodynamic forces and angular moments exerted on the rigid body can be denoted by ${}_{\mathcal{B}}\mathbf{f}$ and ${}_{\mathcal{B}}\boldsymbol{\tau}$, respectively. The vehicle's mass and inertial tensor are represented by m and I, respectively. The inertial tensor takes the form of a diagonal matrix ${}^{\mathcal{B}}_{\mathcal{B}}\mathrm{I} = \mathrm{diag}(I_{xx}, I_{yy}, I_{zz})$ to reflect the symmetries of the geometry.

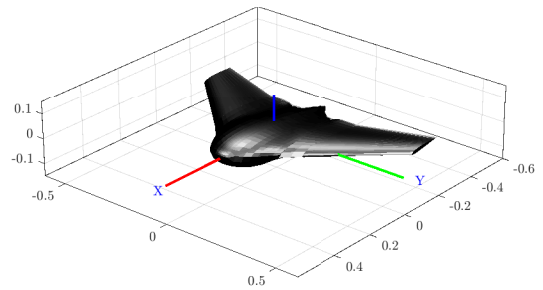

Fig. 2: Visualization of the nominal fixed wing UAS design along with the definition of the body reference system.

$$m\,{}_{\mathcal{B}}\dot{\mathbf{v}} = {}_{\mathcal{B}}\mathbf{f} - mg\,{}_{\mathcal{W}}\mathbf{e}_z \tag{5a}$$

$${}_{\mathcal{B}}\mathrm{I}\,{}_{\mathcal{B}}\dot{\boldsymbol{\omega}} = {}_{\mathcal{B}}\boldsymbol{\tau} - {}_{\mathcal{B}}\boldsymbol{\omega} \times {}_{\mathcal{B}}\mathrm{I}\,{}_{\mathcal{B}}\boldsymbol{\omega} \tag{5b}$$

The state of the rigid body, represented by the vector $\mathbf{x} \in \mathbb{R}^{12}$, encompasses the position and velocity of the center of mass, as well as the minimal representation of its orientation and the angular velocities with respect to the local frame.

$$\mathbf{x} = \begin{bmatrix} {}^{\mathcal{W}}_{\mathcal{B}}\mathbf{p}^\top & \mathbf{q}^\top & {}^{\mathcal{W}}_{\mathcal{B}}\mathbf{v}^\top & {}^{\mathcal{B}}_{\mathcal{B}}\boldsymbol{\omega}^\top \end{bmatrix}^\top \in \mathbb{R}^{12}$$

The aerodynamics of the wing and control surfaces and it propulsion systems generate the force and angular moment, which rely on the control input $\mathbf{u}$ and the design vector $\mathbf{d}$.

B. Aerodynamic Parametrization

Conventionally the input to the FW-UAS system is determined by the propulsion system and the control surfaces. We consider a single propeller tailless fixed wing system with two elevons δ_1 and δ_2 that simultaneously perform the task of the conventional elevator and aileron (Fig. 2). For electric propulsion systems, the motor dynamics are much faster than the rigid body dynamics and aerodynamics. Therefore, it is assumed that propulsion system control can be achieved instantaneously. Furthermore, the thrust vector generated by the propeller is taken proportional to the squared rotor RPM ω. Similarly, control surface actuation is assumed to to occur instantaneously. As such, the control input vector is defined as

$$\mathbf{u} = \begin{bmatrix} \omega & \delta_1 & \delta_2 \end{bmatrix}^\top \in \mathbb{R}^3$$

Consequently, the forces and moments can be expressed as linear combinations of control inputs. The aerodynamic forces are assumed to be made up out of two components: the thrust force, which is assumed to be aligned with ${}_{\mathcal{B}}\mathbf{e}_x$, and the wing induced force, corresponding to the lift and drag force. No side force is assumed to be present. The torque components are assumed to be fully determined by the control surfaces.

$${}_{\mathcal{B}}\mathbf{f} = (k_T\omega^2 - k_D v\,{}_{\mathcal{B}}\mathbf{v}_x)\,{}_{\mathcal{B}}\mathbf{e}_x + k_L v\,{}_{\mathcal{B}}\mathbf{v}_z\,{}_{\mathcal{B}}\mathbf{e}_z \tag{6a}$$

$${}_{\mathcal{B}}\boldsymbol{\tau} = k_{l,\delta} v\,{}_{\mathcal{B}}\mathbf{v}_x(\delta_1 - \delta_2)\,{}_{\mathcal{B}}\mathbf{e}_x + k_{m,\delta} v\,{}_{\mathcal{B}}\mathbf{v}_x(\delta_1 + \delta_2)\,{}_{\mathcal{B}}\mathbf{e}_y + k_{n,\delta} v\,{}_{\mathcal{B}}\mathbf{v}_x(\delta_1 - \delta_2)\,{}_{\mathcal{B}}\mathbf{e}_z \tag{6b}$$

With $k_L = q\partial_v C_L$ the drag force coefficient according to ϕ-theory using the Buckingham π theory motivated conventional lift coefficient C_D [19]. Furthermore, $q = {}^1\!/_2\rho S$, with ρ the density of air and S the wetted surface of the UAS. Similarly, $k_L = q\partial_v C_L$ corresponds to the lift force coefficient, $k_{l,\delta} = qb\partial^2_{v,\delta} C_L$ corresponds to the roll moment coefficient due to elevon deflection δ with b the span-wise distance from the center of gravity to the centroid of the control surface, $k_{m,\delta} = qc\partial^2_{v,\delta} C_L$ corresponds to the pitch moment coefficient due to elevon deflection with c the chord-wise distance from the center of gravity to the centroid of the control surface and $k_{n,\delta} = qb\partial^2_{v,\delta} C_D$ corresponds to the yaw moment coefficient due to elevon deflection.

C. Differential Flatness

One can demonstrate that the FW-UAS exhibits differential flatness using the position and yaw of the system as flat coordinates, as shown in [20].

$$\mathbf{s} = \begin{bmatrix} {}^{\mathcal{W}}_{\mathcal{B}}\mathbf{p}^\top & \gamma \end{bmatrix}^\top \in \mathcal{S} \subset \mathbb{R}^4$$

We briefly summarize the approach by which Tal et al. derived the flat dynamics [20]. From Eq. 6a it can be observed that no lateral forces are present ${}_{\mathcal{B}}\mathbf{f}_y = 0$, which can be justified from the observation that the FW-UAS under consideration has no vertical surfaces (Fig. 2). From this observation, rotating ${}^{\mathcal{W}}\mathbf{f}$ around $\psi\,{}_{\mathcal{W}}\mathbf{e}_z$ from which ϕ can be readily obtained. Eq. 5a and Eq. 6a can now be solved for θ and ω. The angular velocity and angular acceleration can be determined by applying the derivative operation twice on the expression for attitude. This expression is a function of velocity $\dot{\mathbf{p}}$, acceleration $\ddot{\mathbf{p}}$, jerk $\dddot{\mathbf{p}}$, snap $\ddddot{\mathbf{p}}$, yaw ψ, yaw rate $\dot{\psi}$, and yaw acceleration $\ddot{\psi}$. The moment can then be calculated by inverting Eq.5b, which allows for the determination of rotor speeds and flap deflections using Eq.6b. The resulting expressions are too tedious to be presented here. We refer to Tal et al. [20] for a step by step derivation.

Two differential operators, Φ and Ψ, can now be formulated to transform respectively the flat coordinate vector, $\mathbf{s}$, to the state vector, $\mathbf{x} = \Phi[\mathbf{s}]$, and the control input vector, $\mathbf{u} = \Psi[\mathbf{s}]$. One may observe that $\boldsymbol{\tau}$ is a function of the second-order time derivative of the generalized coordinates, ${}^{\mathcal{W}}_{\mathcal{B}}\mathbf{p}$ and $\mathbf{q}$, which are again a function of the second derivative of the flat output trajectory, $\ddot{\mathbf{s}}$. Consequently, the control input is reliant on the fourth-order derivative of the flat output, $\ddddot{\mathbf{s}}$ and should be considered to guarantee seamless control.

D. Aerodynamic solver

In this paper, aerodynamic coefficients of a UAS design are evaluated using Drela's *Athena Vortice Lattice* (AVL) method [21]. AVL is based on potential flow theory, which assumes inviscid, irrotational, and incompressible flow field, resulting in the Navier-Stokes equations that describe the flow around the UAS reducing to the Laplace equation. To induce lift, an irrotational vortex is introduced, and its influence can be determined using Biot-Savart's law. In two-dimensional potential flow, lift can be modeled by introducing a vortex core. In three dimensions, however, the Helmholtz theorem must be satisfied, which enforces that each vortex is closed. This results in the formation of a *horseshoe vortex* that is closed at infinity by a starting vortex. The linear nature of the Laplace equation allows for the assessment of aerodynamic derivatives through chain differentiation.

Within the framework of a two-dimensional panel method, the airfoil surface and wake trajectory are partitioned into N_p panels. In each panel, a linear vorticity distribution is introduced and across the surface constant source strength is defined of which the values are determined by solving a set of equations that enforce flow tangency at each panel and compel the Kutta condition to be met, which states that the flow over the upper and lower surfaces of the airfoil must come together smoothly at the trailing edge. The Vortice Lattice method can be considered as a three-dimensional extension of the panel method, and it corresponds to a discretized formulation of the Prandtl lifting line theory, in which a lifting surface is represented by a zero-thickness sheet. In each panel, a horseshoe vortex is defined and quantified by its strength. To close the set of equations, it is imposed that the flow is parallel to the surface.

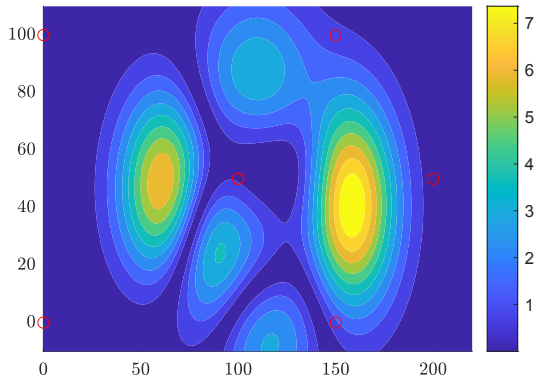

Fig. 3: Top view contour visualization of the flight domain in m. *Red circles represent the target (spatial position constraints) at* $5\mathrm{m}$ *height. The inlet and outlet location are respectively found at* $(0, 0)\mathrm{m}$ *and* $(0, 100)\mathrm{m}$. *The inlet and outlet velocities are determined by the trajectory optimization routine, along with the flight duration.*

IV. Validation Experiment

We specify here the details of the mission that was considered, the design parameterisation of the FW-UAS and document the result of our co-design architecture.

A. Mission specifications and performance metrics

For our lower level trajectory optimization problem we specified a set of targets that should touch the optimized trajectory such that a challenging surveying flight trajectory is provoked (Fig. 3). We define two mission objectives to respectively pursue efficiency and effectiveness. For each of the mission objectives we require the trajectory to minimize a contribution of 3 terms. The complexity of generating aggressive flight trajectories arises from the challenge in enforcing control input constraints, such as motor speed and flap deflection limits, in the flat output space. To address this difficulty, widely adopted algorithms for trajectory generation in the differential flat output space of quadcopter dynamics resort to minimizing snap, which represents the fourth derivative of position and yaw acceleration. This optimization process effectively reduces the demand for control moment, thereby increasing the feasibility of the trajectory and ensuring that control input limits are met [20]. The third term in the respective efficiency and effectiveness objective is the energy expenditure due to thrust and the time spend on the mission.

$$l_1 = w_1 || {}^{\mathcal{W}}_{\mathcal{B}}\ddddot{\mathbf{p}} ||^2 + w_2 ||\ddot{\gamma}||^2 + w_3\omega^2 \tag{7a}$$

$$l_2 = w_1 || {}^{\mathcal{W}}_{\mathcal{B}}\ddddot{\mathbf{p}} ||^2 + w_2 ||\ddot{\gamma}||^2 + w_4 \tag{7b}$$

with $w_1 = 10^{-4}$, $w_2 = 10^{-2}$, $w_3 = 10^{-3}$ and $w_4 = 10^{-1}$. Furthermore, it is enforced that the angle of attack α and sideslip angle β respectively do not exceed $15°$ and $5°$ to avoid stall and ensure the validity of the dynamic model. The thrust is also limited to 25N. In this study, a B-spline basis of order $d = 6$ with 8 equidistant knots ($m = 7$) is employed over the interval $[0, 5]$ to yield 13 basis functions. This is combined with a 4-dimensional flat coordinate space to produce a 52-dimensional trajectory vector. To initialize the trajectory optimization problem, a Fourier series that approximates the targets is utilized and fitted onto the B-spline basis.

For our upper level design optimization problem we pursue the simultaneous minimization of the third terms of the two trajectory optimization objectives. This implies that during every iteration of the multi-objective Bayesian optimization routine the trajectory optimization problem is solved for each objective and a surrogate is built for each of the respective third terms. Furthermore, for each design AVL also provided the stability derivatives $\partial_\alpha C_m$ and $\partial_\beta C_n$, which should be respectively smaller and larger than zero in order for the UAS to be longitudinally and directionally stable. This is included in the BO framework by means of a probability of feasibility approach [22]. This implies that additionally two surrogates constraints are built and the probability that a newly proposed design meets these requirements is multiplied with the acquisition function obtained from the surrogates of the objectives.

The optimization routine is initiated through the evaluation of a *design of experiments* (DoE). In this work a *Latin Hypercube Sampling* (LHS) approach is followed with $d_{\mathbf{d}} \times 11 - 5$ elements. The space-fillingness of the LHS is quantified through a maximin-criterion and maximized. The optimization is stopped when 100 additional designs have been evaluated. The acquisition function, which guides the selection of the next infill, is maximized during every iteration using a *genetic algorithm* (GA) with a population size of $1e3$ and $1e2$ generations.

B. Design parameters and initialization

The FW-UAS being examined in this study exhibits a *blended wing body* (BWB) design, which enhances its aerodynamic performance, and a tailless configuration, resulting in a swept wing to ensure the aircraft maintains its tendency to return to its equilibrium state. The traditional wing parameterization typically used in aerodynamic conceptual design is employed here [23]. The following parameters are fixed: the chord length of the wing at the fuselage, denoted by c_r, is set at 0.3m. The fuselage is modeled as a lifting body with width set at 0.2m, and the total span of the UAS is set at 1m. The following parameters are taken as design variables through which the performance of the UAS is optimized: first, the taper ratio of the wing λ, which corresponds to the ratio of the chord at the tip to the chord at the root $\lambda = c_t/c_r$. Second, the sweep angle of the wing Λ, which is defined as the angle between the leading edge projected on the xy-plane and the y-axis in the body frame. Third, the wing twist γ, which refers to the rotation of the tip in reference to the root of the lifting surfaces. Fourth and final, the fraction of the control surface that can be tilted to initiate maneuvers, denoted as f_C.

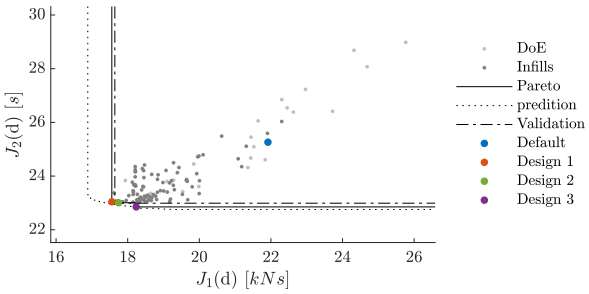

Fig. 4: Pareto front after the final iteration of the multi-objective mission-specific design procedure. The NSGA-II prediction of the Pareto front on the surrogates is presented along with the validation of this front. Furthermore, the DoE is presented along with the infills which migrate towards the Pareto front, indicating the effectiveness of the acquisition function. Finally, the default design and three designs on the Pareto are highlighted.

- Taper ratio wing: $\lambda \in [0.05, 1.00]$
- Sweep angle wing: $\Lambda \in [0^o, 45^o]$
- Twist angle wing: $\gamma \in [-5^o, 5^o]$
- Fraction control surface: $f_C \in [0, 1]$

This results into a design vector of dimensions 4. The extremes of the taper/sweep combinations are shown on the front page. During the trajectory optimization, the coefficients k_L, k_D, k_l, k_m and k_n are kept constant and obtained from the AVL model [21] for the setting where the fixed-wing UAS operates at cruise conditions: $\alpha = 6°$ and $v = 22\text{m/s}$. We assume, following the work of Tal et al. that $\partial_v C_L \approx \partial_\alpha C_L$, $\partial_v C_D \approx 2C_L \partial_v C_L / \pi e AR$, $\partial^2_{v,\delta} C_L \approx f_C \partial_v C_L$ and $\partial^2_{v,\delta} C_D \approx f_C \partial_v C_D$ with e and AR respectively corresponding to the Oswald efficiency factor and the aspect ratio. Despite its coarseness, this approximation enables the exploration of the novel framework and the baseline design. The following parameters are used $m = 2.50\text{kg}$, $I_{xx} = 8.35 \times 10^{-3}\text{kgm}^2$, $I_{yy} = 1.18 \times 10^{-2}\text{kgm}^2$, $I_{zz} = 1.99 \times 10^{-2}\text{kgm}^2$.

The baseline design is selected to closely resemble the commercially available Gatewing UX5 (Fig. 2) [24]. The resulting values of the reference design are $k_L = 6.14 \times 10^{-2}\text{kg/m}$, $k_D = 2.66 \times 10^{-4}\text{kg/m}$, $k_{l,\delta} = 4.29 \times 10^{-2}\text{kg}$, $k_{m,\delta} = 1.46 \times 10^{-2}\text{kg}$ and $k_{n,\delta} = 2.3 \times 10^{-3}\text{kg}$.

C. Results and discussion

The results of the multi-objective mission specific design is a Pareto front of optimized designs that outperform the standard design in various metrics (Fig. 4). Three designs on the front are selected for closer inspection, which are summarized together with the baseline geometry in Table. I.

TABLE I: Overview of co-designs

	λ [−]	Λ [°]	γ [°]	f_C [−]	J_1 [kNt]	J_2 [t]
Default	0.470	37.499	-4.500	0.700	21.917	25.262
Design 1	0.203	41.765	0.225	1.000	17.557	23.044
Design 2	0.157	42.723	-0.595	1.000	18.211	22.986
Design 3	0.167	45.000	-6.083	1.000	18.239	22.852

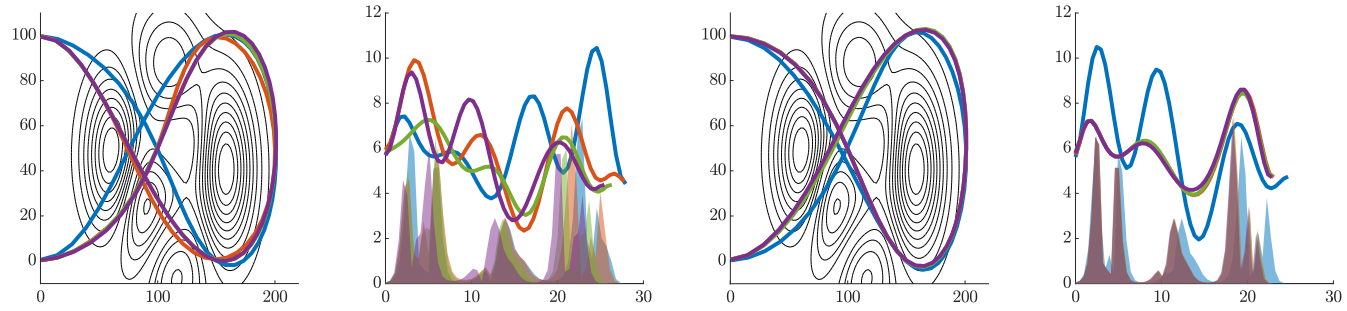

(a) Top view for the efficiency objective *(b) Side view for the efficiency objective* *(c) Top view for the effectiveness objective* *(d) Side view for the effectiveness objective*

Fig. 5: Optimal mission trajectories for the default and optimal designs. Using the same color code as Fig. 4

Upon careful examination of the taper ratios, it was determined that smaller tip chords were favored in optimal designs. However, no clear trend was identified. The sweep angle was maximized to enhance performance, but slightly reduced for improved efficiency. The backward sweep of the wings was also necessitated by the requirement for longitudinal and directional stability, which were both positively impacted by the wing sweep. A similar trend was observed for the wing twist, which had a limited impact on performance objectives but a significant contribution to stability requirements. The control fraction was maximized in all designs, owing to its direct relationship to the torque coefficients and the aircraft's ability to execute sharp maneuvers. However, the potential for stall during these maneuvers could limit its practical application, as the models used in the analysis lack the capability to accurately predict this scenario.

The optimized trajectories of the default and optimized designs are depicted in Fig. 5. The side views of the efficiency-driven trajectories reveal substantial variations among the different designs, while the distinctions among the effectiveness-driven trajectories is less pronounced. Upon examining the top view of the trajectories, a higher degree of consistency can be discerned across the designs, with the intersection point of the trajectories being the most salient difference. The considerable disparities observed between the trajectories, despite modest differences in design, highlight the importance of concurrent design methodologies and suggest the need for further investigation in this area.

V. Conclusion and Outlook

In this paper, we presented a model-based multi-objective dynamical system design strategy. The co-design optimization approach, which combines design and trajectory optimization, was examined in a nested formulation and enhanced with multiple objectives. This was achieved through the integration of the multi-objective formulation of Bayesian optimization that simultaneously minimizes multiple criteria through the use of a dedicated acquisition function, with a dedicated trajectory optimization methodology relying on the differential flatness of the dynamic system considered.

The dynamical design problem used as a case study was the mission-specific design of fixed-wing unmanned aerial systems, with the objective of simultaneously minimizing its energy expenditure while performing a surveying task as quickly as possible. The results demonstrate optimized designs that outperform the standard design in different metrics. A trade-off between levels of efficiency and effectiveness can be observed, thus allowing the designer to select an optimal design geometry based on the application type of the unmanned aerial vehicle and proving the effectiveness of the dynamic design approach.

The framework is limited to tasks that are highly repetitive; a change in working conditions might lead to suboptimal performance. Therefore, a topic of ongoing research is the pursuit of robustness in designs for changing tasks and/or environment. To realize this, a probabilistic approach is foreseen in which the overall performance to be optimized is set to correspond with the sum of a set of basic flight maneuvers. This is a subject of ongoing research. Furthermore, accuracy increase is pursued through the incorporation of Gaussian process interpolators on the systems dynamics level. By doing so we pursue the ability to increase the accuracy of the simulator without increasing the computational cost of the optimization routine.

Acknowledgment

The authors gratefully acknowledge the funding by the Research Foundation-Flanders (FWO), Belgium, through the Junior Post-Doctoral fellowship of Jolan Wauters and the Energy Transition Fund (ETF) project BORNE. The computational resources (Stevin Supercomputer Infrastructure) and services used in this work were provided by the VSC (Flemish Supercomputer Center), funded by Ghent University, Belgium, FWO and the Flemish Government — department EWI, Belgium.

References

[1] J. R. R. A. Martins and A. B. Lambe, "Multidisciplinary design optimization: A survey of architectures," *AIAA Journal*, vol. 51, no. 9, pp. 2049–2075, 2013.

[2] D. R. Herber and J. T. Allison, "Nested and simultaneous solution strategies for general combined plant and control design problems," *Journal of Mechanical Design*, vol. 141, no. 1, 2018.

[3] J. Wauters, T. Lefebvre, and G. Crevecoeur, "Comparative study of co-design strategies for mission-specific design of quadcopters using differential flatness and bayesian optimization," in *IEEE/ASME (AIM) International Conference on Advanced Intelligent Mechatronics*. IEEE, Conference Proceedings, pp. 703–709.

[4] E. Todorov, "A convex, smooth and invertible contact model for trajectory optimization," in *2011 IEEE International Conference on Robotics and Automation*, Conference Proceedings, pp. 1071–1076.

[5] E. A. Tal and S. Karaman, *Global Trajectory-tracking Control for a Tailsitter Flying Wing in Agile Uncoordinated Flight*, ser. AIAA AVIATION Forum. American Institute of Aeronautics and Astronautics, 2021.

[6] S. Ha, S. Coros, A. Alspach, J. Kim, and K. Yamane, "Computational co-optimization of design parameters and motion trajectories for robotic systems," *The International Journal of Robotics Research*, vol. 37, no. 13-14, pp. 1521–1536, 2018.

[7] J. Whitman and H. Choset, "Task-specific manipulator design and trajectory synthesis," *IEEE Robotics and Automation Letters*, vol. 4, no. 2, pp. 301–308, 2018.

[8] M. Toussaint, J.-S. Ha, and O. S. Oguz, "Co-optimizing robot, environment, and tool design via joint manipulation planning," in *2021 IEEE International Conference on Robotics and Automation (ICRA)*. IEEE, 2021, pp. 6600–6606.

[9] B. Shahriari, K. Swersky, Z. Wang, R. P. Adams, and N. d. Freitas, "Taking the human out of the loop: A review of bayesian optimization," *Proceedings of the IEEE*, vol. 104, no. 1, pp. 148–175, 2016.

[10] C. E. Rasmussen and C. K. I. Williams, *Gaussian Processes for Machine Learning*. the MIT Press, 2006.

[11] P. S. Palar, L. R. Zuhal, T. Chugh, and A. Rahat, *On the Impact of Covariance Functions in Multi-Objective Bayesian Optimization for Engineering Design*, ser. AIAA SciTech Forum. American Institute of Aeronautics and Astronautics, 2020.

[12] M. L. Stein, "A kernel approximation to the kriging predictor of a spatial process," *Annals of the Institute of Statistical Mathematics*, vol. 43, no. 1, pp. 61–75, 1991.

[13] I. Couckuyt, T. Dhaene, and P. Demeester, "ooDACE toolbox: a flexible object-oriented kriging implementation," *J. Mach. Learn. Res.*, vol. 15, no. 1, pp. 3183–3186, 2014.

[14] Z. Ugray, L. Lasdon, J. Plummer, F. Glover, J. Kelly, and R. Martí, "Scatter search and local nlp solvers: A multistart framework for global optimization," *INFORMS Journal on Computing*, vol. 19, no. 3, pp. 328–340, 2007.

[15] J. Nocedal and S. J. Wright, *Numerical Optimization*, ser. Springer Series in Operations Research and Financial Engineering. Springer, 2006.

[16] I. Couckuyt, D. Deschrijver, and T. Dhaene, "Fast calculation of multiobjective probability of improvement and expected improvement criteria for pareto optimization," *Journal of Global Optimization*, vol. 60, no. 3, pp. 575–594, 2014.

[17] F. Stoical, V.-M. Ivănuşcă, I. Prodan, and D. Popescu, "Obstacle avoidance via b-spline parametrizations of flat trajectories," in *2016 24th Mediterranean Conference on Control and Automation (MED)*. IEEE, 2016, pp. 1002–1007.

[18] D. Mellinger and V. Kumar, "Minimum snap trajectory generation and control for quadrotors," in *2011 IEEE international conference on robotics and automation*. IEEE, 2011, pp. 2520–2525.

[19] L. R. Lustosa, F. Defaÿ, and J.-M. Moschetta, "Global singularity-free aerodynamic model for algorithmic flight control of tail sitters," *Journal of Guidance, Control, and Dynamics*, vol. 42, no. 2, pp. 303–316, 2018.

[20] E. Tal, G. Ryou, and S. Karaman, "Aerobatic trajectory generation for a vtol fixed-wing aircraft using differential flatness," *arXiv preprint arXiv:2207.03524*, 2022.

[21] M. Drela and H. Youngren, "AVL 3.27," 2017. [Online]. Available: http://web.mit.edu/drela/Public/web/avl/

[22] A. Forrester, A. Sóbester, and A. Keane, *Engineering Design via Surrogate Modelling: A Practical Guide*. Wiley, 2008.

[23] A. Sóbester and A. Forrester, *Aircraft Aerodynamic Design: Geometry and Optimization*. Wiley, 2014.

[24] J. Wauters, I. Couckuyt, N. Knudde, T. Dhaene, and J. Degroote, "Multi-objective optimization of a wing fence on a uav using surrogate-derived gradients," *Structural and Multidisciplinary Optimization*, vol. 61.